Geochemistry
Geophysics
Geosystems

G³

Article
Volume 13, Number 5
19 May 2012
Q05Z41, doi:10.1029/2012GC004063
ISSN: 1525-2027

Published by AGU and the Geochemical Society

Ferromagnetic resonance characterization of greigite (Fe_3S_4), monoclinic pyrrhotite (Fe_7S_8), and non-interacting titanomagnetite ($Fe_{3\text{-}x}Ti_xO_4$)

Liao Chang
National Oceanography Centre, University of Southampton, European Way, Southampton SO14 3ZH, UK

Research School of Earth Sciences, Australian National University, Canberra, ACT 0200, Australia

Paleomagnetic Laboratory "Fort Hoofddijk," Department Earth Sciences, Utrecht University, Budapestlaan 17, NL-3584 CD Utrecht, Netherlands (l.chang@uu.nl)

Michael Winklhofer
Department of Earth and Environmental Science, Ludwig-Maximilians University, Theresienstrasse 41, D-80333 Munich, Germany

Andrew P. Roberts
National Oceanography Centre, University of Southampton, European Way, Southampton SO14 3ZH, UK

Research School of Earth Sciences, Australian National University, Canberra, ACT 0200, Australia

Mark J. Dekkers
Paleomagnetic Laboratory "Fort Hoofddijk," Department Earth Sciences, Utrecht University, Budapestlaan 17, NL-3584 CD Utrecht, Netherlands

Chorng-Shern Horng
Institute of Earth Sciences, Academia Sinica, PO Box 1-55, Nankang, Taipei 11529, Taiwan

Lei Hu and Qianwang Chen
Hefei National Laboratory for Physical Sciences at Microscale and Department of Materials Science and Engineering, University of Science and Technology of China, Hefei 230026, China

[1] Ferromagnetic resonance (FMR) spectroscopy has become an increasingly useful tool for studying the magnetic properties of natural samples. Magnetite (Fe_3O_4) is the only magnetic mineral that has been well characterized using FMR. This limits the wider use of FMR in rock magnetism and paleomagnetism. In this study, we applied FMR analysis to a range of magnetic minerals, including greigite (Fe_3S_4), monoclinic pyrrhotite (Fe_7S_8), magnetically non-interacting titanomagnetite ($Fe_{3\text{-}x}Ti_xO_4$), and synthetic magnetite chains to constrain interpretation of FMR analysis of natural samples and to explore applications of FMR spectroscopy. We measured the FMR signatures of a wide range of well-characterized samples at the X- and Q-bands. FMR spectra were also simulated numerically to compare with experimental results. The effects of magnetic anisotropy, mineralogy, domain state, and magnetostatic interactions on the FMR spectra are discussed for all studied minerals. Our experimental and theoretical analyses of magnetically non-interacting tuff samples and magnetically interacting chains enable quantitative assessment of contributions of magnetostatic interactions and magnetic anisotropy to the FMR spectra. Our results also

Copyright 2012 by the American Geophysical Union

indicate that intact magnetosomes are a unique system with distinct FMR signatures. While FMR analysis is useful for characterizing magnetic properties of natural samples, care is needed when making interpretations because of overlaps in a range of FMR signatures of different magnetic minerals with different magnetic properties. Our analyses will help to constrain such interpretations in rock magnetic studies.

Components: 10,900 words, 10 figures, 1 table.

Keywords: ferromagnetic resonance; greigite; magnetostatic interactions; pyrrhotite; titanomagnetite.

Index Terms: 1512 Geomagnetism and Paleomagnetism: Environmental magnetism; 1540 Geomagnetism and Paleomagnetism: Rock and mineral magnetism; 3929 Mineral Physics: NMR, Mossbauer spectroscopy, and other magnetic techniques.

Received 20 January 2012; **Revised** 17 April 2012; **Accepted** 19 April 2012; **Published** 19 May 2012.

Chang, L., M. Winklhofer, A. P. Roberts, M. J. Dekkers, C.-S. Horng, L. Hu, and Q. Chen (2012), Ferromagnetic resonance characterization of greigite (Fe_3S_4), monoclinic pyrrhotite (Fe_7S_8), and non-interacting titanomagnetite ($Fe_{3-x}Ti_xO_4$), *Geochem. Geophys. Geosyst.*, *13*, Q05Z41, doi:10.1029/2012GC004063.

Theme: Magnetism From Atomic to Planetary Scales: Physical Principles and Interdisciplinary Applications in Geosciences and Planetary Sciences

1. Introduction

[2] Ferromagnetic resonance (FMR) (also termed electron paramagnetic resonance (EPR) for paramagnetic materials and termed electron spin resonance (ESR) in general) is a spectroscopic technique that has recently been applied to problems in rock magnetism and paleomagnetism. For example, it has been used to characterize intracellular magnetosome chains and detect their fossil remains in sediments [e.g., *Weiss et al.*, 2004; *Kopp et al.*, 2006a, 2007, 2009; *Fischer et al.*, 2008; *Faivre et al.*, 2010; *Kind et al.*, 2011; *Roberts et al.*, 2011a; *Gehring et al.*, 2011a], to assess magnetic anisotropy and magnetic interactions [e.g., *Kopp et al.*, 2006b; *Fischer et al.*, 2008; *Mastrogiacomo et al.*, 2010; *Gehring et al.*, 2011b], to trace iron biogeochemistry in sediments [*Maloof et al.*, 2007], and for environmental magnetic interpretations [e.g., *Pawse et al.*, 1998; *Crook et al.*, 2002; *Fischer et al.*, 2007; *Roberts et al.*, 2011a]. Therefore, FMR analysis has the potential to become a standard tool in rock magnetic studies. Despite its increasing application, FMR signatures remain unknown for most magnetic minerals, except for magnetite (Fe_3O_4). This limits its potential in rock magnetism and paleomagnetism.

[3] In this study, we performed FMR analyses on a range of magnetic minerals, including magnetic iron sulfides (greigite (Fe_3S_4) and monoclinic pyrrhotite (Fe_7S_8)), non-interacting titanomagnetite ($Fe_{3-x}Ti_xO_4$) and synthetic magnetite chains, to constrain interpretation of FMR analysis of natural samples and to explore applications of FMR spectroscopy. Iron sulfide minerals are widespread in nature and are considered to be the most important minerals in ore deposits. The thiospinel greigite and monoclinic pyrrhotite are two important magnetic iron sulfide phases [e.g., *Pearce et al.*, 2006]. Greigite commonly forms in anoxic diagenetic sedimentary environments [see *Roberts et al.*, 2011b, and references therein], and as a biomineralization product [e.g., *Konhauser*, 1998; *Bazylinski and Frankel*, 2004; *Suzuki et al.*, 2006]. Pyrrhotite is common as an authigenic mineral in sediments [e.g., *Weaver et al.*, 2002], as a detrital mineral in sediments [e.g., *Horng and Roberts*, 2006], and in igneous and metamorphic rocks [e.g., *Rochette*, 1987; *Horng and Roberts*, 2006]. Magnetic iron sulfide minerals are also commonly present in extraterrestrial materials in the solar system [e.g., *Rochette et al.*, 2001]. Iron sulfides are important carriers of remanent magnetizations and therefore significantly contribute to paleomagnetic and paleoenvironmental records in many geological settings. In this study, we analyzed a wide range of well-characterized greigite and pyrrhotite samples. We also analyzed a set of standard samples from the Tiva Canyon (TC) ash flow tuff that contains non-interacting single-domain (SD) titanomagnetite ($Fe_{3-x}Ti_xO_4$) grains. The TC Tuff has long been of interest in rock magnetism because of its narrow magnetic grain size distribution and well dispersed magnetic particles that lack magnetostatic interactions [e.g., *Schlinger et al.*, 1991; *Rosenbaum*, 1993; *Worm and Jackson*, 1999; *Roberts et al.*, 2000; *Till et al.*, 2011]. These tuff samples appear therefore ideal for studying the FMR signal of an

interaction-free system other than bacterial cells. Finally, we analyzed synthetic magnetite chains to compare measured FMR signatures with those from intact magnetite-producing magnetotactic bacteria and magnetofossils.

2. Samples

[4] The pure synthetic and natural greigite samples analyzed here (Figures 1a and 1b) have been subjected to detailed magnetic characterization previously [*Chang et al.*, 2007, 2008, 2009a, 2009b; *Roberts et al.*, 2011b]. The pure synthetic greigite samples (labeled "SYN-XXX") were prepared by hydrothermally reacting ferric chloride ($FeCl_3 \cdot 6H_2O$) with thiourea (CH_4N_2S) and formic acid (HCOOH) at 170°C for eight hours [*Tang et al.*, 2007; *Chang et al.*, 2008]. After synthesis, the greigite samples were sealed in small glass sample vials and were stored in a desiccator to prevent oxidation. These synthetic greigite samples contain nearly equi-dimensional crystalline particles, of mostly cubo-octahedral morphology, in the 10 μm size range. These synthetic greigite samples are dominated by pseudo-single-domain (PSD)/multidomain (MD) magnetic properties [*Chang et al.*, 2007, 2008]. The natural greigite samples are iron sulfide nodules from the Valle Ricca section near Rome [*van Dongen et al.*, 2007] and from the Lower Gutingkeng Formation in southwestern Taiwan [*Jiang et al.*, 2001] (and are labeled "Italy" and "Taiwan," respectively). Greigite is the only magnetic phase in these natural samples, which have SD magnetic properties. Scanning electron microscope (SEM) observations indicate that these samples contain equi-dimensional greigite grains (mostly cubo-octahedral) with lengths of several hundred nanometers [*Roberts et al.*, 2011b]. The grain size distribution of these samples has not been determined because the greigite crystals are too small to be accurately resolved with SEM instruments.

[5] Sample "EOR2" is a natural hydrothermal pyrrhotite sample collected from mine dumps at Ortano on the east coast of Elba [*Dekkers*, 1988]. This pyrrhotite sample was obtained by crushing the pyrrhotite-bearing rocks and magnetically concentrating the pyrrhotite. The pyrrhotite was then sieved. This sample contains equidimensional pyrrhotite grains in the 100–150 μm size range [*Dekkers*, 1988]. Samples "9–47" and "20–131" are pyrrhotite-bearing metamorphic rocks from Taiwan (C.-S. Horng, Metamorphic pyrrhotite as a tracer for denudation of orogenic belts, manuscript in preparation, 2012). These samples represent the parent material from which detrital pyrrhotite is supplied to marginal marine basins in Taiwan [*Horng and Roberts*, 2006; *Horng and Huh*, 2011]. SEM observations indicate that these samples contain hexagonal-shaped and irregular pyrrhotite crystals in the micrometer size range. Sample "syn_ph" is a synthetic pyrrhotite sample formed by heating the synthetic greigite sample in argon [*Chang et al.*, 2008]. X-ray diffraction, thermomagnetic and low-temperature measurements indicate that this sample contains single-phase monoclinic pyrrhotite.

[6] The titanomagnetite-bearing samples ("TC05_7.1," "TC05_7.2," and "TC05_9.0") are from the TC ash flow tuff at Yucca Mountain, southern Nevada [e.g., *Schlinger et al.*, 1991; *Rosenbaum*, 1993; *Worm and Jackson*, 1999]. These samples were provided by the Institute for Rock Magnetism, University of Minnesota, and contain dominantly non-interacting SD titanomagnetite particles [e.g., *Carter-Stiglitz et al.*, 2006; *Jackson et al.*, 2006; *Till et al.*, 2011]. Transmission electron microscope (TEM) observations indicate that these samples contain significantly elongated and well-dispersed titanomagnetite grains (Figure 1c) [e.g., *Rosenbaum*, 1993; *Till et al.*, 2011]. Using thermal-fluctuation tomography [*Jackson et al.*, 2006], the magnetic grain size for sample TC05_9.0 was determined to have a length to width ratio of ~0.3, and a length of 87 nm [e.g., *Carter-Stiglitz et al.*, 2006]. High-temperature susceptibility measurements indicate Curie temperatures of ~550°C for these samples, which indicate that the magnetic mineralogy is dominated by Ti-poor titanomagnetite (TM10) [e.g., *Rosenbaum*, 1993; *Carter-Stiglitz et al.*, 2006; *Jackson et al.*, 2006; *Till et al.*, 2011].

[7] Synthetic magnetite chain samples were prepared following the method of *Liu and Chen* [2008]. Reagents used include 0.5 g of ferrocene ($Fe(C_5H_5)_2$) (98%), 0.75 g of polyvinylpyrrolidone (PVP), and 12.0 g of dry ice (99.9%). Hydrothermal reaction occurred in a 20 ml steel autoclave at 450°C for 800 min. After reaction, the solution was cooled to room temperature naturally and the remaining CO_2 was vented. The synthetic product was then washed alternately with toluene and ethanol several times, and dried at 60°C in air for several hours. The final product is composed of linear chains of SD magnetite (octahedra) that range from 40 to 120 nm, covered by a thin amorphous carbon coating (Figure 1d).

3. Methods

[8] In a typical EPR experiment, a sample is subjected to a DC magnetic field and microwave

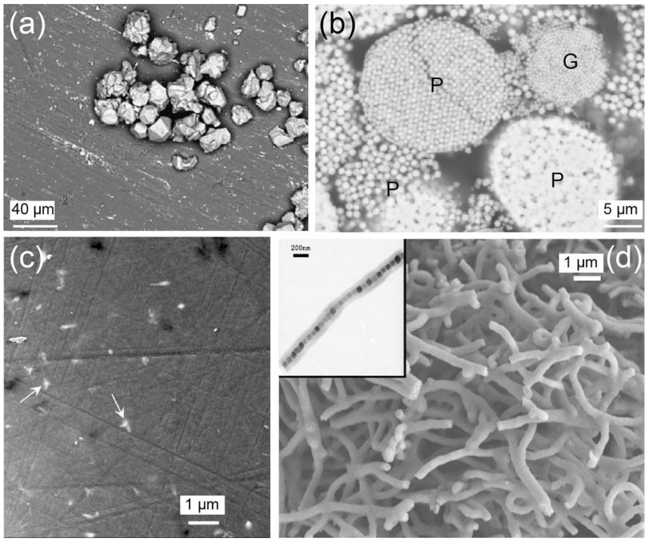

Figure 1. SEM images of selected studied samples with illustration of the morphologies of the magnetic grains. (a) Pure synthetic greigite [*Chang et al.*, 2008]. (b) Sedimentary greigite from Italy [*van Dongen et al.*, 2007]. "P" and "G" indicate pyrite (FeS_2) and greigite crystal clusters, respectively. (c) The TC tuff (reproduced from *Till et al.* [2011]). White arrows indicate the dispersed needle-like titanomagnetite crystals within a non-magnetic matrix. (d) Synthetic magnetite chains (reproduced from *Liu and Chen* [2008]). The inset is a TEM image of a linear chain of synthetic SD magnetite crystals aligned along the $\langle 111 \rangle$ crystallographic axis in magnetite. The thin layer surrounding the chain is a carbon coating.

radiation and is placed in a resonating cavity that can absorb photons generated by a microwave radiation source. The microwave energy can be absorbed by the sample due to the Zeeman effect that splits the energy of the unpaired electron within an atom or molecule in a magnetic field. In a magnetic field, the spin of the unpaired electron can align either along or in the opposite direction to the magnetic field. A resonant absorption condition occurs when the incident photon energy is equal to the energy separation between the two electronic energy levels. The resonance condition is given by:

$$h\nu = g\mu_B B, \tag{1}$$

where $h = 6.626 \times 10^{-34}$ Js is Planck's constant, ν is the microwave frequency, B is the intensity of the magnetic field and $\mu_B = 9.274 \times 10^{-24}$ J/T is the Bohr magneton. In FMR, absorption of microwave energy is due to exchange-coupled spin assemblages precessing coherently around the local effective field vector B_{eff} when the Larmor precession frequency associated with B_{eff} is equal to the microwave frequency ν. This process produces intense and broad signals [*Griscom*, 1980; *Kittel*, 1996]. The resonance condition in FMR is also given by equation (1), where B is replaced by B_{eff}. The effective magnetic field B_{eff} is the vector sum of the applied field and internal fields due to sample geometry, magnetocrystalline anisotropy, stress-induced anisotropy, and magnetic interactions (dipolar and exchange interactions). The FMR signature therefore contains much useful information about the magnetic properties of samples. A detailed description of the FMR theory is given by *Kittel* [1996]. A detector measures the change in FMR absorption as a function of a sweeping magnetic field produced by an electromagnet (Figure 2a). FMR spectra are usually measured and displayed as the first derivative of absorption (Figure 2b). This enhances the signal-to-noise ratio [e.g., *Pawse et al.*, 1998] and magnifies the fine structure of the FMR absorption signal. The FMR spectra can be used to quantify some simple magnetic systems, e.g., a non-interacting SD assemblage. Other systems, e.g., assemblages with magnetostatic interactions, so far can only be understood in a general way.

[9] We use the following parameters to describe the FMR spectra (Figure 2). B_{eff} is the zero-crossing field in the derivative spectra, which is also the maximum absorption field in the integrated spectra. The effective g value (g_{eff}) is given by $g_{eff} = h\nu/\mu_B B_{eff}$. B_{low}, B_{high}, ΔB_{FWHM} and A are defined in a typical absorption spectrum (integration of the first derivative spectrum) (Figure 2a) [e.g., *Weiss et al.*, 2004; *Kopp et al.*, 2006a, b]. B_{low} and B_{high} are the magnetic fields where the absorption is half the maximum value at the low- and high-field ends,

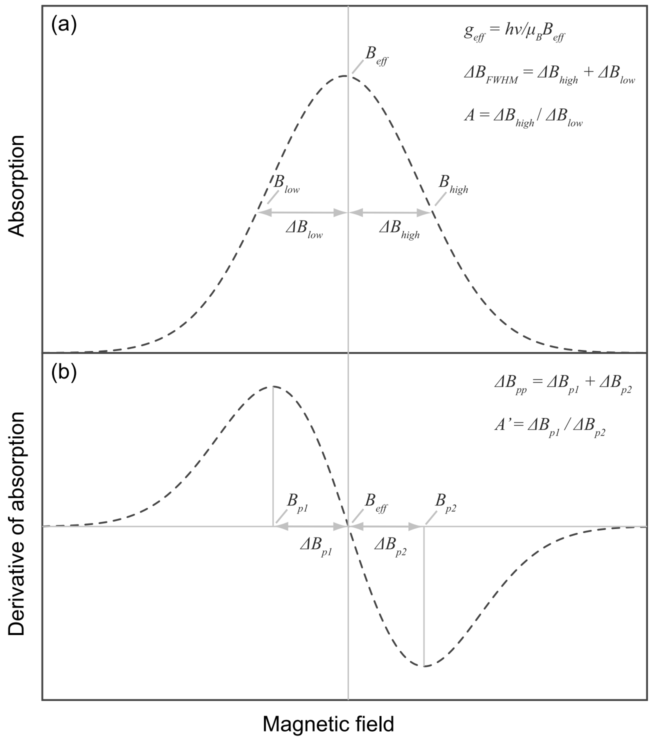

Figure 2. Illustration of parameters commonly determined from FMR spectra. (a) A simple FMR absorption spectrum with Gaussian line shape and (b) the corresponding derivative absorption spectrum.

respectively, of the absorption peak. ΔB_{low} and ΔB_{high} are the low- and high-field linewidths, respectively. ΔB_{FWHM} is the sum of ΔB_{low} and ΔB_{high} and is the width of the absorption peak at half of its maximum value. The asymmetry ratio A is defined as $A = \Delta B_{high}/\Delta B_{low}$. We also define a set of FMR parameters in a typical first derivative spectrum (Figure 2b) that are similar to those used by *Griscom* [1974] and *Fischer et al.* [2008]. B_{p1} and B_{p2} are the magnetic fields at the maximum and minimum peaks, respectively. The peak-to-peak linewidth ΔB_{pp} is the distance between B_{p1} and B_{p2}, and $A' = \Delta B_{p1}/\Delta B_{p2} = (B_{eff} - B_{p1})/(B_{p1} - B_{eff})$.

[10] The FMR spectra were measured using an X-band Bruker EMX micro spectrometer and a Q-band Bruker E500 FMR spectrometer at the School of Chemistry, the University of Manchester, and at the Research School of Earth Sciences, Australian National University. For each measurement, small samples (from several mg to a few tens of mg) were loaded into FMR glass tubes. For X-band measurements, we set the microwave frequency at ~9.4 GHz and the microwave power at ~0.632 mW. All spectra were integrated over several magnetic field sweeps from 0 to 700 mT. At the Q-band, the microwave frequency was set at ~34 GHz and the microwave power at ~0.12 mW. Field scans were made from 10 to 1410 mT and from 600 to 2000 mT for Q-band measurements. There is not much useful information below 600 mT, therefore we only present data from the 600–2000 mT scan at Q-band.

[11] FMR spectra were simulated using the model described by *Charilaou et al.* [2011]. Elongated crystals were modeled as prolate ellipsoids of revolution, with aspect ratio $q = c/a$, where c and a denote long and short major axes, respectively. The demagnetization factors along these axes are $N_c < N_a$, and $\Delta N = N_a - N_c$. For cubic minerals and for particles elongated along a ⟨100⟩ axis (hard axis), the cubic magnetocrystalline anisotropy energy density is given by:

$$w^{XL}{}_{100} = \frac{K_1}{16}\sin^2\vartheta\left(9 + 7\cos(2\vartheta) - 2\cos(4\varphi)\sin^2\vartheta\right),$$

where (ϑ, φ) denotes the polar and azimuthal angle of the magnetization with respect to the long particle axis. For particles elongated along the ⟨110⟩ (intermediate axis) and ⟨111⟩ (easy axis) axes, the respective expressions are given by:

$$w^{XL}{}_{110} = \frac{K_1}{4}\Big(\cos^4\vartheta - 2\sin^2\vartheta\cos^2\vartheta\cos^2\varphi + \left[\cos^4\varphi + \sin^2(2\varphi)\right]\sin^4\vartheta + \sin^2\varphi\sin^2(2\vartheta)\Big),$$

and

$$w^{XL}{}_{111} = \frac{K_1}{12}\left(3\sin^4\vartheta + 4\cos^4\vartheta + 4\sqrt{2}\sin^3\vartheta\cos\vartheta\cos(3\varphi)\right).$$

For each of the three crystallographic scenarios, we computed FMR powder spectra for several axial ratios q, following the approach of *Charilaou et al.* [2011], who dealt with crystals elongated along the $\langle 111\rangle$ axis. By taking advantage of symmetry relationships, we can restrict the applied field range to $\vartheta_H \in [0, 90°]$, $\varphi_H \in [0, 45°]$ for the $\langle 100\rangle$ case, to $\vartheta_H \in [0, 90°]$, $\varphi_H \in [0, 90°]$ for the $\langle 110\rangle$ case, and to $\vartheta_H \in [0, 90°]$, $\varphi_H \in [0, 60°]$ for the $\langle 111\rangle$ case. For numerical computation, the (ϑ_H, φ_H) interval is approximated by a discrete grid with equidistant spacing in φ_H (5° mesh size) and equidistant in the cos ϑ_H (0.02 mesh size). For each point on the (ϑ_H, φ_H) grid, the resonance condition is evaluated and the resulting resonance field (a delta peak) is convolved with a Lorentzian of 20 mT half-width field at half maximum.

[12] We use the following magnetic parameters for our FMR simulations. For magnetite, we use a saturation magnetization (M_s) of 470 kA/m and a first-order cubic magnetocrystalline anisotropy constant (K_1) of -12 kJ/m^3 [*Kakol and Honig*, 1989]. For TM10, we use M_s of 435 kA/m and K_1 of -23 kJ/m^3 determined with the torque method [*Syono and Ishikawa*, 1963]. Strictly speaking, K_1 values obtained from torque magnetometer measurements represent stress-free K_1' values and need to be corrected for magnetostriction to obtain the intrinsic strain-free K_1 [*Ye et al.*, 1994]. However, we do not know whether the titanomagnetite crystals in the TC Tuffs are strain-free. Regardless, the difference between K_1' and K_1 is small for low-x titanomagnetite. From equation (9) in *Ye et al.* [1994] and the magnetostriction data for $x = 0.1$ [*Syono and Ishikawa*, 1963], we find that $K_1' - K_1 = \sim 3$ kJ/m^3, so that $K_1 = -20$ kJ/m^3, in accordance with the K_1 data obtained by *Kakol et al.* [1991] and interpolated for TM10.

[13] While the magnetocrystalline anisotropy energy of ideal monoclinic pyrrhotite is characterized by a purely sixfold symmetry in the basal plane [e.g., *Martín-Hernández et al.*, 2008], our pyrrhotite samples are not ideal and therefore are best described by a uniaxial (twofold symmetry) anisotropy in the basal plane. We therefore modeled monoclinic pyrrhotite with uniaxial magnetocrystalline anisotropy in the basal plane. In this case, the expression for the magnetocrystalline anisotropy energy is given by *Bin and Pauthenet* [1963]:

$$w = K_1\sin^2\vartheta'\sin^2\varphi' + K_3\cos^2\vartheta' + K_4\cos^4\vartheta',$$

where ϑ' is the angle of the magnetization with respect to the hard [001] direction and φ' is the azimuthal angle of the magnetization projected onto the easy (001) plane, where $\varphi_H' = 0$ defines the easy axis in the plane. The anisotropy model with purely sixfold symmetry in the basal plane will be dealt with in more detail in a separate paper. The room temperature magnetocrystalline anisotropy coefficients for monoclinic pyrrhotite are $K_4 = 32.2 \times 10^5$ J/m^3, $K_3 = 1.18 \times 10^5$ ^{1}J/m^3, $K_1 = 0.35 \times 10^5$ J/m^3 [*Bin and Pauthenet*, 1963; *Martín-Hernández et al.*, 2008]. These parameters were used as they appear to reflect typically real samples. We simulate equant particles because the shape anisotropy (M_s = 80 kA/m) is of minor importance compared to magnetocrystalline anisotropy for pyrrhotite.

4. Results and Discussion

4.1. Greigite

4.1.1. FMR Spectra at X-Band

[14] Room temperature X-band FMR spectra for selected greigite samples are presented in Figure 3 and FMR parameters are listed in Table 1. Pure synthetic greigite samples give rise to a single absorption line with maximum and minimum absorption peaks at ~130 and ~330 mT, respectively, with ΔB_{FWHM} of around 200 mT (Figure 3a). The peak intensity of low-field absorption is consistently larger than that of the high-field peak. These synthetic samples have high g_{eff} values (2.9–3.1), which is consistent with the expectation that MD assemblages typically have large g_{eff} values well above the free electron value of 2 [e.g., *Weiss et al.*, 2004]. The spectra are asymmetric with A values larger than 1 (Table 1). The large g_{eff}, ΔB and A values can be explained by enhanced low-field absorption due to absorption in magnetic domains within MD particles in directions different to that of the applied field. The small nonzero absorption near zero field (Figure 3a) may also be a reflection of a MD effect. Compared to the pure synthetic greigite samples, the sedimentary greigite samples have different FMR spectra (Figure 3b): g_{eff} values are much reduced (2.02), linewidth is lower (~180 mT) and A is less than 1 (0.7)

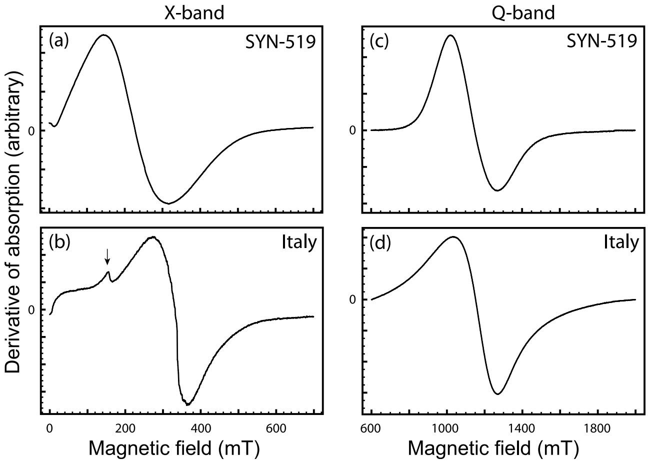

Figure 3. Room temperature FMR spectra for selected greigite samples measured at (a and b) X-band and (c and d) Q-band. The small absorption near zero field for pure synthetic greigite samples at X-band (Figure 3a) may be caused by MD effects, which disappear at Q-band (Figure 3c). The small absorption peak indicated by the arrow at ~160 mT in Figure 3b is due to absorption of paramagnetic Fe^{3+} ions within the sedimentary greigite sample.

Table 1. Room Temperature FMR Parameters of the Samples Measured in This Study

			FMR Parameters Defined in the Absorption Spectra								
Minerals	Sample Name	Band	B_{eff} (mT)	g_{eff}	B_{low} (mT)	B_{high} (mT)	ΔB_{low} (mT)	ΔB_{high} (mT)	A	ΔB_{FWHM} (mT)	α
Greigite	SYN-627	X	214.4	3.13	132.7	328.6	82	114	1.398	196	0.43
Greigite	SYN-519	X	227.8	2.95	132.7	340.3	95	113	1.183	208	0.40
Greigite	SYN-709	X	225.7	2.98	142.5	348.8	83	123	1.479	206	0.45
Greigite	Italy	X	332.4	2.02	228.4	407.6	104	75	0.724	179	0.30
Pyrrhotite	EOR2	X	284.2	2.36	248.2	320.4	36	36	1.008	72	0.24
Pyrrhotite	9–47	X	331.7	2.02	301.7	368.6	30	37	1.229	67	0.27
Pyrrhotite	20–131	X	330.7	2.03	288.7	372.8	42	42	1.002	84	0.25
Titanomagnetite	TC05_7.1	X	330.5	2.03	184.5	427.0	146	97	0.661	243	0.35
Titanomagnetite	TC05_7.2	X	328.0	2.05	189.0	427.3	139	99	0.714	238	0.35
Titanomagnetite	TC05_9.0	X	325.3	2.06	194.8	426.5	131	101	0.775	232	0.36
Magnetite	chain	X	300.9	2.23	184.0	411.0	117	110	0.942	227	0.38
Magnetite	diluted chain	X	308.5	2.18	188.4	410.4	120	102	0.849	222	0.36
Greigite	SYN-706	Q	1165.6	2.08	1035.0	1329.8	131	164	1.257	295	0.50
Greigite	SYN-504	Q	1145.1	2.12	1007.7	1320.9	137	176	1.279	313	0.52
Greigite	Taiwan	Q	1156.0	2.10	968.0	1312.3	188	156	0.831	344	0.48
Pyrrhotite	syn-ph	Q	1199.1	2.03	1065.1	1371.5	134	172	1.286	306	0.52

			FMR Parameters Defined in the Derivative Spectra								
Minerals	Sample Name	Band	B_{eff} (mT)	g_{eff}	B_{p1} (mT)	B_{p2} (mT)	ΔB_{p1} (mT)	ΔB_{p2} (mT)	A'	ΔB_{pp} (mT)	α
Greigite	SYN-627	X	214.6	3.13	142.9	297.9	72	83	1.162	155	0.35
Greigite	SYN-519	X	227.9	2.95	143.8	317.2	84	89	1.062	173	0.35
Greigite	Italy	X	332.5	2.02	272.9	366.2	60	34	0.565	93	0.19
Pyrrhotite	EOR2	X	284.0	2.36	263.9	303.3	20	19	0.958	39	0.20
Pyrrhotite	9–47	X	332.1	2.02	309.5	366.6	23	35	1.530	57	0.32
Pyrrhotite	20–131	X	331.0	2.03	309.1	366.2	22	35	1.612	57	0.33
Greigite	SYN-706	Q	1169.3	2.08	1048.0	1286.7	121	117	0.968	239	0.40
Greigite	SYN-504	Q	1148.2	2.12	1017.2	1269.6	131	121	0.926	252	0.40
Greigite	Taiwan	Q	1152.0	2.11	1037.0	1268.9	115	117	1.017	232	0.40
Pyrrhotite	syn-ph	Q	1199.4	2.03	1100.0	1234.0	99	35	0.348	134	0.19

(Table 1). The low-field peak intensity is also smaller than that of the high-field peak. The small absorption peak at ∼155 mT (Figure 3b) corresponds to a g value of 4.3, which is typical of paramagnetic high-spin Fe^{3+} in a low symmetry environment, such as in feldspars [*Hofmeister and Rossman*, 1984], and here is related to paramagnetic Fe^{3+} within the sediments [e.g., *Kopp et al.*, 2006a].

4.1.2. FMR Spectra at Q-Band

[15] We measured several greigite samples at Q-band (Figures 3c and 3d). All measured synthetic and natural greigite samples have a single absorption line, while the spectra for natural samples are more spread out. The spectrum for a pure synthetic greigite sample indicates a higher maximum peak intensity compared to the minimum peak intensity, while this is opposite for the spectrum from a natural greigite sample. These observations are similar to X-band results. Because of the higher microwave frequency at Q-band, the resonance condition occurs at much higher magnetic fields, i.e., ∼1150 mT (Table 1). g_{eff} values are almost indistinguishable for different samples at Q-band (2.08–2.12). The A value for synthetic greigite is higher than 1 (∼1.3), while for sedimentary greigite it is lower than 1 (0.8).

4.1.3. Interpretation

[16] To interpret the FMR signature of greigite, we first discuss the nature of the studied greigite samples and consider the simple case of a non-interacting, equidimensional SD particle assemblage. SEM observations indicate that sedimentary greigite-bearing rocks often contain nearly equidimensional cubo-octahedral greigite crystals (Figure 1b) [e.g., *Jiang et al.*, 2001; *Roberts and Weaver*, 2005; *Hüsing et al.*, 2009; *Sagnotti et al.*, 2010; *Roberts et al.*, 2011b]. SEM images of the studied natural greigite confirm the presence of equidimensional greigite crystals (Figure 1b) [*van Dongen et al.*, 2007; *Roberts et al.*, 2011b]. Contributions from shape anisotropy compared to magnetocrystalline anisotropy can therefore be ignored. Dominance of magnetocrystalline anisotropy in sedimentary greigite is also confirmed by hysteresis data from natural greigite samples, which often indicate hysteresis squareness ratios higher than 0.5 [e.g., *Roberts*, 1995; *Sagnotti and Winkler*, 1999; *Vasiliev et al.*, 2007; *Roberts et al.*, 2011b]. The measured synthetic greigite samples are also composed of equidimensional cubo-octahedral crystals, although elongated particles (e.g., plates and prisms) were occasionally observed (Figure 1a) [*Chang et al.*, 2008]. The natural greigite samples are dominated by SD properties, while the synthetic samples are dominated by PSD/MD grains [*Chang et al.*, 2007, 2008, 2009b]. These PSD/MD grains will have a significant effect on the X-band spectra, for example, large g_{eff} values at X-band are observed. However, because the magnetization of greigite saturates at ∼300 mT [e.g., *Dekkers and Schoonen*, 1996; *Roberts et al.*, 2011b], the large scanning field range of 600 to 2000 mT during Q-band FMR measurements is high enough to saturate the magnetization. This is one reason that we carried out Q-band measurements to saturate the PSD/MD grains so that they effectively display SD behavior. For magnetic interactions, SEM observations indicate that sedimentary greigite often forms in close-packed particle clusters (Figure 1b) [e.g., *Jiang et al.*, 2001; *Roberts and Weaver*, 2005], which produce strong magnetostatic interactions [e.g., *Roberts et al.*, 2000, 2006; *Vasiliev et al.*, 2007]. During sample preparation, we mixed the synthetic greigite powders with eicosane ($C_{20}H_{42}$) to dilute the magnetic grains. Although this procedure can significantly reduce magnetostatic interactions, many magnetic particles will still clump and produce magnetic interactions [*Kopp et al.*, 2006a].

[17] Greigite has cubic crystal symmetry. K_1 for greigite has been inferred to be positive at room temperature [e.g., *Yamaguchi and Wada*, 1970; *Bazylinski et al.*, 1995]. However, this inference needs further investigation. Non-interacting SD greigite with magnetocrystalline anisotropy should give rise to FMR spectra with $A < 1$ and $g_{eff} < 2.12$ if $K_1 > 0$, and with $A > 1$ and $g_{eff} > 2.12$ if $K_1 < 0$ [e.g., *Griscom*, 1974; *Weiss et al.*, 2004]. X-band FMR measurements on some sedimentary greigite samples yield g_{eff} values close to 2 and A ∼0.7 (Table 1). The observed large g_{eff} value above 2 is probably caused by magnetostatic interactions. Currently, we cannot quantitatively measure the effects of magnetostatic interactions on FMR spectra for greigite due to the difficulty in obtaining greigite samples without magnetostatic interactions. In principle, magnetostatic interactions can broaden FMR spectra and shift g_{eff} to higher values [e.g., *Valstyn et al.*, 1962; *Kopp et al.*, 2006b]. FMR parameters with $A < 1$ and $g_{eff} < 2.12$ have been suggested to provide strong evidence for magnetite magnetosome chain structures within samples [*Weiss et al.*, 2004]. Our FMR measurements indicate that diagenetic greigite (Figure 1b) can sometimes also have $A < 1$ and $g_{eff} < 2.12$. Despite the large overlap in A and g_{eff}

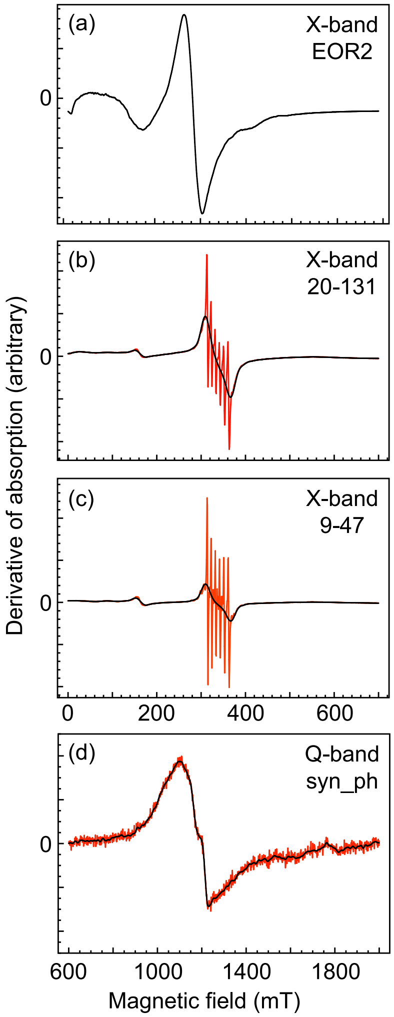

Figure 4. Room temperature FMR spectra for a range of pyrrhotite samples at (a–c) X-band and (d) Q-band. The red curves in Figures 4b and 4c are experimental data, which contain multiple sharp absorption lines that originate from Mn^{2+} ions. A FFT smoothing approach has been applied to remove the sharp Mn^{2+} lines and data noise in Figure 4d, and to give the broad absorption lines (black lines).

values for diagenetic greigite and magnetite magnetosome chains, which might indicate ambiguity in their discrimination, we observe a large difference in their B_{eff} values (Table 1). Combined with other FMR characteristics for magnetite magnetosome chains (e.g., multiple low-field absorption peaks), FMR analysis should still enable effective discrimination between them. On the other hand, no FMR measurements have been reported for greigite magnetosomes [*Vasiliev et al.*, 2008]. Such direct measurements on greigite magnetosomes are much needed to determine whether they give rise to distinctive FMR spectra.

4.2. Monoclinic Pyrrhotite

[18] Most pyrrhotite samples were measured at X-band with one sample at Q-band (Figure 4 and Table 1). At X-band, sample "EOR2" has a dominant single absorption line (Figure 4a) with a g_{eff} value of 2.36. A is close to 1, which indicates nearly symmetric absorption spectra. The absorption line is sharp with a narrow peak-to-peak linewidth (39 mT). The small broad peak at low fields may reflect an MD effect. First-order reversal curve results indicate that sample "EOR2" is dominated by MD particles [*Wehland et al.*, 2005], which may contribute to the observed higher g_{eff} value. Complex FMR spectra were observed for samples "20–131" and "9–47" (Figures 4b and 4c). The small peak at ~160 mT and the multiple sharp lines are characteristic of the absorption of Fe^{3+} and Mn^{2+}, respectively [e.g., *Kopp et al.*, 2006a]. The sharp Mn^{2+} lines overprint the FMR signal for pyrrhotite, but can be readily removed by Fast Fourier Transform (FFT) smoothing [*Roberts et al.*, 2011a]. After FFT smoothing, the background FMR signal is clear (Figures 4b and 4c). ΔB_{pp} is ~57 mT and g_{eff} values are close to 2 (Table 1). At Q-band, the g_{eff} value for the synthetic pyrrhotite sample is 2.03 and ΔB_{pp} is ~134 mT.

[19] We simulated FMR spectra for equant pyrrhotite powders at different bands (Figure 5). When solving the FMR equation for ideal monoclinic pyrrhotite at X-band frequencies (9.4 GHz), solutions occur only at ($\varphi'_H = \pm\pi/2$), with low-field absorption at 840 mT at $\vartheta'_H = \pm\pi/2$ (i.e., in the (110) plane) and high-field absorption at 30.5 T at $\vartheta'_H = 0$ (i.e., along the [001] axis), which results in a mean g_{eff} value of 0.72 ($B_{eff} = 0.92$ T) for the two-dimensional powder FMR spectrum obtained by averaging the B_{eff} ($\cos\vartheta'_H$; $\varphi'_H = \pm\pi/2$) curve, convoluted with a Lorentzian intrinsic line shape. At Q-band frequencies (34 GHz), the directional range that satisfies the resonance conditions becomes larger (φ'_H within 10 degrees of ±90°). While the FMR "powder" spectrum has clear gaps because of the narrow directional range within which resonance events can occur (blue curve in Figure 5), the obtained $g_{eff} = 2.07$ ($B_{eff} = 1.17$ T) is nevertheless in good agreement with our Q-band data for the synthetic sample ($g_{eff} = 2.03$, $B_{eff} = 1.2$ T). At W-band frequencies (68 GHz), all field orientations produce at least one resonance event. The corresponding powder FMR derivative spectrum (magenta curve in Figure 5) has a strongly asymmetric shape and a $g_{eff} = 12.90$ ($B_{eff} = 0.377$ T). The g-values are 0.22 for the high-field event (along the hard [001] axis) and 14.6 for the

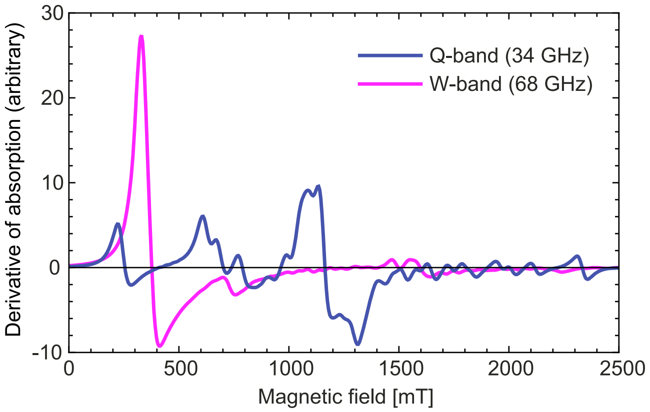

Figure 5. Derivative FMR absorption spectra simulated for a sample consisting of randomly oriented monoclinic pyrrhotite crystals probed at 34 GHz (blue) and 68 GHz (magenta). The atypical shape of the Q-band spectrum is due to the fact that only a subset of crystals satisfies the resonance condition.

low-field resonance event along the easy axis ($\varphi'_H = 0$ in the (110) plane). Such pronounced anisotropy in the g-value is commonly observed in strongly uniaxial antiferromagnets [e.g., *Koonce et al.*, 1971].

[20] Published FMR data for monoclinic pyrrhotite are sparse. *Mikhlin et al.* [2002] measured FMR spectra for an air-ground pyrrhotite sample, but no clear FMR signature could be extracted from their spectrum. *Fujimura and Torizuka* [1956] measured the FMR spectrum of a pyrrhotite single crystal. They observed an extremely large linewidth measured in the easy direction of magnetization, which they attributed to line broadening caused by possible microcrystals within their sample. No resonance was observed when the applied field deviated >10° from the crystallographic c-plane probably because of the large magnetic anisotropy energy along the c-axis in monoclinic pyrrhotite [*Fujimura and Torizuka*, 1956]. Our FMR modeling indicates that FMR absorption in powdered monoclinic pyrrhotite is small at low frequencies. This is mainly due to the large uniaxial anisotropy in monoclinic pyrrhotite, i.e., the large magnetocrystalline anisotropy (the K_4 term) along the c-axis. This large anisotropy only allows resonance to occur at much larger frequencies, i.e., at W-band. At X- and Q-bands, resonance events do not occur in general, but only for some particular directions. This explains why we observed extremely weak FMR signals (note the strong paramagnetic Mn^{2+} signals in Figures 4b and 4c) despite the fact that the measured pyrrhotite samples are magnetically strong. The X-band spectra of the natural samples probably reflect real structural features (e.g., magnetic domain walls, intergrowths, and twinning etc.) and impurity effects, rather than intrinsic properties of pyrrhotite. Our results demonstrate that pyrrhotite is not a good FMR absorber, at least at the low frequencies (i.e., X-band) that are commonly used for FMR measurements. FMR analysis of more samples and oriented pyrrhotite single crystals and angular dependent FMR spectra are needed to better constrain the FMR signature of pyrrhotite.

4.3. Non-interacting Titanomagnetite and Synthetic Magnetite Chains

4.3.1. FMR Spectra at X-Band

[21] Similar FMR spectra are observed for all three TC tuff samples at X-band (Figure 6). These spectra are extremely asymmetric and contain three low-field maxima and two high-field minima. g_{eff} values are low and range from 2.03 to 2.06 (Table 1), which is close to that of a free electron and for the applied field parallel to an easy axis of magnetization in magnetite [*Bickford*, 1950]. ΔB_{FWHM} values are between 232 and 243 mT. A is between 0.66 and 0.76. It should be noted that, although SD grains dominate these tuff samples, small portions of PSD/MD and superparamagnetic (SP) grains are also present [e.g., *Carter-Stiglitz et al.*, 2006; *Jackson et al.*, 2006]. SP grains may contribute to the small peak at ~200 mT and the shoulder near $g = 2$ (Figure 6). This SP contribution should be small as room temperature frequency dependent susceptibility measurements indicate small changes (only ~2–3% per decade) [e.g., *Carter-Stiglitz et al.*, 2006; *Jackson et al.*, 2006]. Because of absence of magnetostatic interactions among the magnetic grains, the observed FMR spectra should be simply a linear superposition of

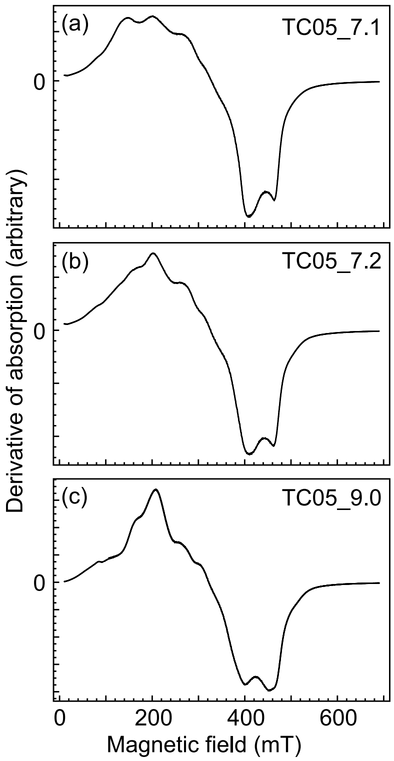

Figure 6. Room temperature X-band FMR spectra for a set of TC tuff samples that contain non-interacting SD titanomagnetite grains.

different components [e.g., *Weiss et al.*, 2004]. The observed FMR spectra should therefore represent mainly the signature of non-interacting SD titanomagnetite.

[22] The FMR spectrum of a synthetic magnetite chain sample (Figure 7) does not contain characteristics of magnetosome chain signatures even though abundant linear magnetite chains are present within the samples (Figure 1d) [*Liu and Chen*, 2008]. FMR parameters for this sample are: A = 0.942, g_{eff} = 2.23, and ΔB_{FWHM} = 227 mT. Diluting this sample with eicosane consistently reduced the FMR parameters to A = 0.849, g_{eff} = 2.18, and ΔB_{FWHM} = 222 mT (Table 1). This reduction in the FMR parameters after dilution is similar to that found by *Kopp et al.* [2006b]. However, despite the dilution, the FMR parameters still do not hint at a magnetite chain structure.

4.3.2. Simulation of X-Band FMR Spectra

[23] The three analyzed TC tuff samples have FMR derivative spectra with a conspicuous high-field double-well feature (at 400 and 460 mT) and a low-field peak at about 220 mT with more or less pronounced side lobes (Figure 6). To our knowledge, such a well-resolved high-field double-well feature has not been observed in published FMR derivative spectra from other geological samples. To study the possible origin of this feature and other FMR signatures, we simulated FMR spectra for $Fe_{3-x}Ti_xO_4$ crystals (x = 0.1, TM10). *Schlinger et al.* [1991] did not observe any obvious unidirectional orientation of precipitated TM10 microcrystals, therefore we here computed powder spectra by isotropically averaging over all directions in space. It is also not known if the titanomagnetite crystals in the TC tuff are elongated along a preferred crystallographic axis [see *Schlinger et al.*, 1991]. We therefore considered three families of preferred elongation axes: $\langle 100 \rangle$, $\langle 110 \rangle$, and $\langle 111 \rangle$.

[24] For simulated FMR spectra of magnetically non-interacting TM10 assemblages with different elongations and along different crystallographic directions ($\langle 100 \rangle$, $\langle 110 \rangle$ and $\langle 111 \rangle$), the low-field peak consistently shifts with increasing particle elongation to lower field values (Figure 8). The more elongated the particles, the smaller is the external magnetic field required to produce resonance for the specific orientation where the external field is parallel to the long particle axis. The low-field peak for particles elongated along the $\langle 110 \rangle$ and $\langle 111 \rangle$ crystallographic axes splits into double peaks with increasing particle elongation. Two low-field peaks are commonly seen in FMR derivative spectra for intact magnetosome chains [*Kopp et al.*, 2006a, 2006b; *Fischer et al.*, 2008], but their spectra lack the distinct double-well feature on the high-field side of the spectrum. For an axial ratio of $q \sim 2$ (with elongation along the $\langle 111 \rangle$ axis), the double-well positions are B = 410 mT and 470 mT, as is the case in the experimental spectra. Particles elongated along the $\langle 110 \rangle$ axis also produce a double-well structure, albeit at different field values. Despite the good agreement in terms of the

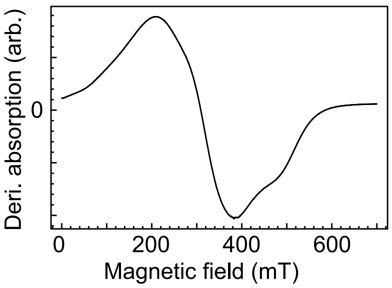

Figure 7. Room temperature X-band FMR spectra for diluted synthetic magnetite chains.

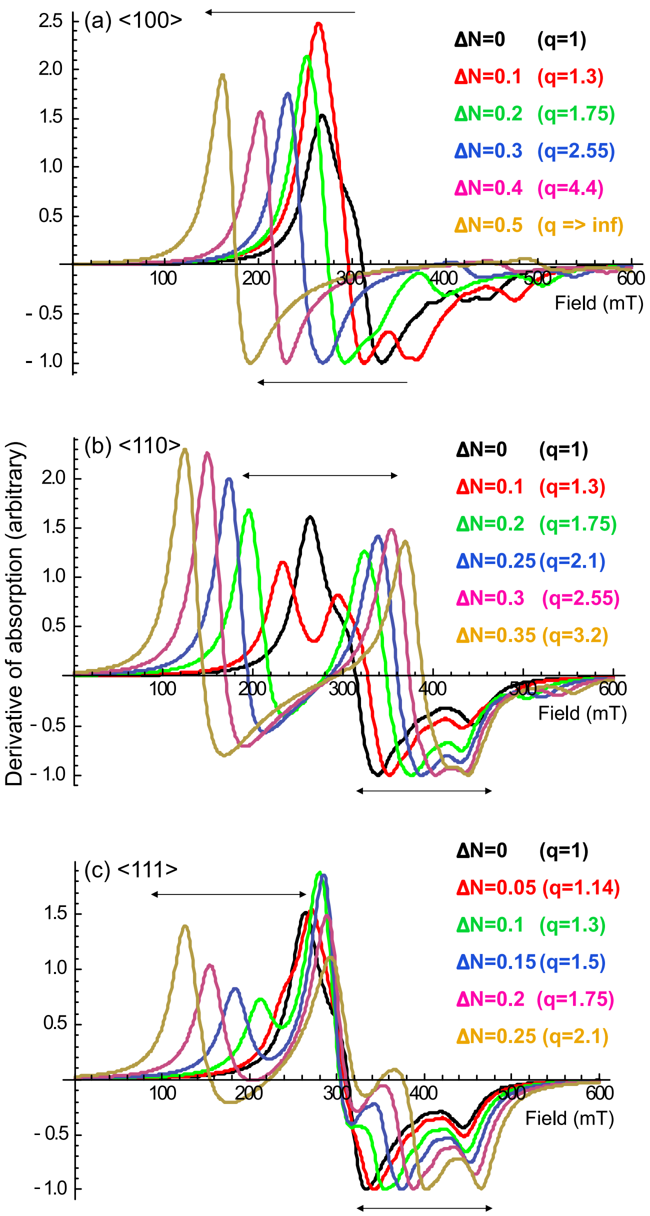

Figure 8. Simulated powder FMR derivative spectra for magnetically non-interacting titanomagnetite (TM10) assemblages at X-band with different axial ratios q (or equivalent ΔN values) for three preferred elongation axes: (a) $\langle 100\rangle$, (b) $\langle 110\rangle$, and (c) $\langle 111\rangle$. In Figure 8a, arrows indicate that increasing particle elongation shifts spectra to lower fields and thus increases g_{eff}. In Figures 8b and 8c, arrows indicate that increasing particle elongation splits the low-field peak into two peaks and the spread between high-field troughs (the well-resolved high-field double-well feature) decreases with increasing particle elongation.

double-well feature, there are significant deviations between simulations and experimental data below 400 mT. In particular, the experimentally observed low-field peak at 200 mT is absent in simulations that correctly reproduce the double-well feature. Absence of the 200 mT peak in an otherwise compatible spectrum rules out elongation along the $\langle 111\rangle$ axes of the TM10 particles in the TC Tuff [*Schlinger et al.*, 1991]. Likewise, a single peak at 200 mT is present in the $q \sim 4.4$ spectrum for the $\langle 100\rangle$ case, however, the high-field spectrum has no suitably located double-well feature. None of the simulated spectra can explain all of the features observed in the experimental data and it is possible that the particles in the TC Tuff are elongated along a crystallographic axis that is different to the three cases simulated here. Use of high-resolution TEM observations would be ideal to resolve this question. Alternatively, in the absence of a single preferred elongation direction, the observed spectra probably represent a more complicated mixture. For example, the experimental spectra have a shallow slope around the effective field (when crossing zero), which is typical of mixture. We also modeled mixtures of grains with different elongation directions and SP grains, which did not give results comparable to the experimental data. This is probably due to the complexity of the studied TC tuff samples, which contain multiple components (different grain elongations and elongation axes). Nevertheless, our modeling results indicate that the lower g_{eff} values of the TC tuff are probably due to significant particle elongation and lack of magnetostatic interactions. The high-field double well feature likely develops due to low-field splitting at significant grain elongation as a result of averaging of simulated spectra over all directions in space (Figure 8). Our modeling indicates that FMR spectra for the TC tuff cannot be fully explained by a comparatively simple magnetic distribution. This is probably because there is not a single-preferred crystallographic direction for particle elongation in the TC tuff samples. This indicates that the TC tuff is still a complicated FMR system, even though it is not affected by magnetostatic interactions.

[25] We also simulated powder FMR derivative spectra at X-band for magnetite chains aligned along the $\langle 111 \rangle$ crystallographic axis (Figure 9) to compare with experimental spectra. Similar to the modeling results of *Charilaou et al.* [2011], magnetite chains can produce FMR spectra with $g_{eff} < 2$, and $A < 1$, and also multiple low-field peaks. The simulations indicate that an effective demagnetization factor ΔN as small as 0.2 is sufficient to explain the high-field peak at 390 mT (compare Figures 7 and 9). However, this simulated spectrum has $g_{eff} < 2$, i.e., the effective field is larger than the isotropic resonance field of 336 mT at X-band. Therefore, to explain the experimentally observed $g_{eff} > 2$ (effective field of 300–310 mT) (Figure 6), a second FMR component centered well below 300 mT has to be added to the synthetic spectrum for non-interacting chains. That broad component does not represent a physical component, but rather a distribution of magnetostatic interactions.

4.3.3. Interpretation

[26] We suggest that the FMR spectra for the TC tuff samples probably represent the complex sum of multiple components. Our modeling results indicate that it is not possible to fit the measured spectra with a single magnetic component. In addition, slight sample heterogeneity due to particle size distribution may also gives rise to high α values (Table 1) and broadening of the low-field side of the spectra (Figure 6). TM10 has a cubic structure with negative K_1. An equidimensional SD assemblage of such particles with no magnetostatic interactions should therefore have $A > 1$ and $g_{eff} > 2.12$, as is the case for magnetite [e.g., *Weiss et al.*, 2004; *Kopp et al.*, 2006b]. Our FMR modeling indicates a g_{eff} value of 2.15 for equidimensional grains (Figure 8). TEM observations indicate that the measured TC tuff samples contain significantly elongated titanomagnetite grains (Figure 1c) [e.g., *Rosenbaum*, 1993; *Till et al.*, 2011]. Such acicular morphology produces strong shape anisotropy. TEM observations also indicate good dispersion among titanomagnetite particles (Figure 1c) [e.g., *Rosenbaum*, 1993; *Till et al.*, 2011], which results in nearly no magnetostatic interactions. Such a non-interacting SD assemblage with strong shape anisotropy can shift absorption to lower fields and produce $A < 1$ and $g_{eff} < 2.12$, and may also produce multiple absorption maxima, as observed in magnetotactic bacteria [e.g., *Weiss et al.*, 2004; *Kopp et al.*, 2006a, 2006b]. These FMR signatures are consistent with our experimental data and simulations. In contrast, basalts containing interacting titanomagnetite grains have high g_{eff} and ΔB values and $A > 1$ [e.g., *Weiss et al.*, 2004]. Our FMR data indicate that the lower FMR parameters (g_{eff}, ΔB and A) for these non-interacting tuff samples compared to those in basalts are probably due to a combination of enhanced shape anisotropy and absence of three-dimensional magnetostatic interactions. While three-dimensional magnetostatic interactions (as in the case of particle clumps) broaden the FMR spectra and shift g_{eff} and A to higher values [e.g., *Kopp et al.*, 2006b], absence of three-dimensional magnetostatic interactions can preserve FMR signatures with $A < 1$, $g_{eff} < 2.12$ and multiple peaks. In contrast to bacterial cells, the synthetic carbon coating surrounding the magnetite chains is too thin to keep the chains from magnetically interacting with each other. This magnetic particle system of closely spaced chains should be seen as clumps, which therefore has both strong shape anisotropy and three-dimensional magnetostatic interactions. Our measurements of this sample demonstrate that three-dimensional magnetostatic interactions can apparently mask the FMR signature of magnetosome chains, which supports

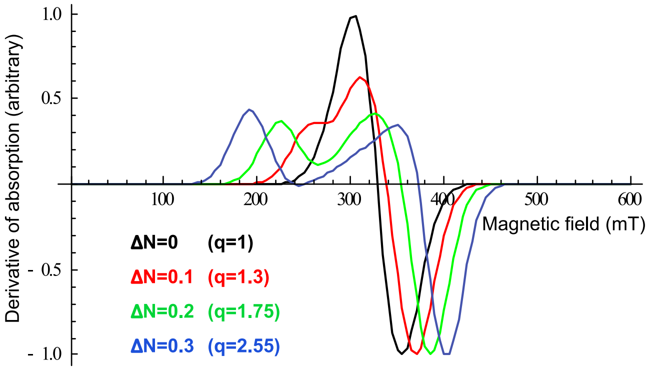

Figure 9. Simulated powder FMR derivative spectra at X-band for magnetite chains aligned along the ⟨111⟩ crystallographic axis with different effective demagnetization factors (ΔN). Each resonance event in the calculations was convolved with a Gaussian linewidth of 20 mT.

previous observations by *Weiss et al.* [2004] and *Kopp et al.* [2006a].

[27] We conclude that the observed multiple absorption maxima with $A < 1$ and $g_{eff} < 2.12$ are due to a combination of strong shape anisotropy and lack of three-dimensional magnetostatic interactions. Enhanced shape anisotropy can be attributed to particle elongation effects (in the case of TC tuff samples) or to one-dimensional magnetostatic interactions due to chain structures (in the case of the intact magnetosomes). Absence of three-dimensional interactions is a result of good dispersion of magnetic particles within the TC tuff samples or to separation of magnetosome chains by bacterial cells or other materials. The overlap of some FMR signatures (i.e., $A < 1$ and $g_{eff} < 2.12$) between magnetotactic bacteria [e.g., *Weiss et al.*, 2004; *Kopp et al.*, 2006a, 2006b, 2007, 2009; *Kind et al.*, 2011; *Gehring et al.*, 2011a; *Roberts et al.*, 2011a] and other types of samples analyzed here suggests that care is needed when using FMR spectroscopy to detect magnetosome chains within samples. Despite the large overlap in A and g_{eff} values that may cause interpretational ambiguity, there is a large difference in B_{eff} values for magnetosome chains compared to other samples (Table 1). For example, the TC tuff samples have much larger B_{eff} values compared to those of intact magnetite magnetosomes [e.g., *Weiss et al.*, 2004; *Kopp et al.*, 2006a, 2006b, 2007, 2009; *Fischer et al.*, 2008; *Roberts et al.*, 2011a]. These distinct FMR signatures should therefore enable discrimination between the different types of magnetic particle assemblage. Our analysis also demonstrates that intact magnetosomes produced by magnetotactic bacteria are a unique model system with distinct FMR signatures [*Weiss et al.*, 2004; *Kopp et al.*, 2006a, 2006b; *Charilaou et al.*, 2011].

5. Summary and Conclusions

[28] The shape of FMR spectra and the values of FMR parameters (such as g_{eff}, ΔB_{FWHM} and A) are sensitive to magnetic mineralogy, magnetic anisotropy (magnetocrystalline, magnetoelastic and shape anisotropy due to crystal morphology and/or to the spatial arrangement of particles), magnetic mineral grain size (SP/MD effects), and magnetostatic interactions. We plot our measured FMR parameters in plots of g_{eff} versus A (Figure 10a) and ΔB_{FWHM} versus A (Figure 10b) following *Weiss et al.* [2004] and *Kopp et al.* [2006a, 2006b]. In a plot of g_{eff} versus A (Figure 10a), some diagenetic greigite samples and the TC tuff samples fall within the region for magnetite magnetosome chains (i.e., $A < 1$ and $g_{eff} < 2.12$). On the other hand, data for the measured samples are more scattered in plots of ΔB_{FWHM} versus A in which values of the parameter α are also shown (Figure 10b). α is an empirical parameter that combines the FMR parameter A and ΔB_{FWHM}. It is defined as $\alpha = 0.17A + 9.8 \times 10^{-4} \Delta B_{\mathrm{FWHM}}$ [*Kopp et al.*, 2006a, 2006b], and is an empirical proxy for σ, the Gaussian broadening factor [*Kopp et al.*, 2006b]. Low values of α and σ imply more homogeneous size, shape and arrangement of particles, which *Kopp and Kirschvink* [2008] interpreted as a fingerprint of natural selection on the biologically controlled mineralization of magnetosomes. Our results support the hypothesis of *Kopp et al.* [2006a, 2006b] that the FMR parameters of $g_{eff} < 2.12$, $A < 1$ and $\alpha < \sim 0.3$ strongly suggest the presence of magnetofossils in sediment samples.

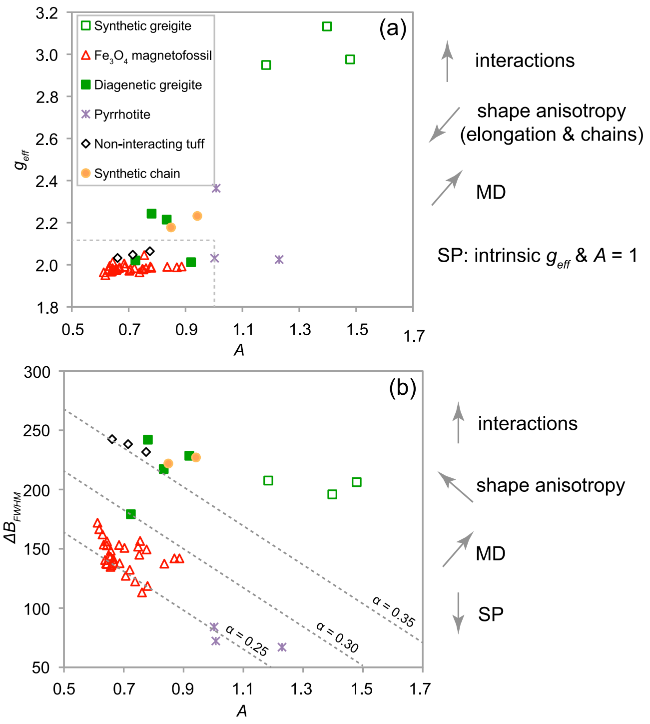

Figure 10. Plots of X-band FMR parameters in (a) a g_{eff} versus A diagram and (b) a ΔB_{FWHM} versus A diagram, following *Weiss et al.* [2004] and *Kopp et al.* [2006a, 2006b]. All data, except for those from magnetite magnetofossils [*Roberts et al.*, 2011a], are from this study. The dashed lines in Figure 10a represent g_{eff} = 2.12 and A = 1. Data from magnetotactic bacteria fall within the region with $A < 1$ and $g_{eff} < 2.12$ [*Weiss et al.*, 2004; *Kopp et al.*, 2006a, 2006b]. The dashed lines in Figure 10b represent contours of the empirical FMR parameter α (see text for a description of α). The effects of variations in different magnetic properties on the FMR parameters are illustrated by arrows on the right. These arrows indicate the general trends of FMR parameters with increasing effects.

[29] Various effects (magnetostatic interactions, domain state and crystal morphology) on FMR parameters are illustrated in Figure 10. In summary, enhanced positive anisotropy (originating either from grain elongation or chain structure) increases ΔB_{FWHM} and decreases g_{eff} and A. Three-dimensional magnetostatic interactions produce higher g_{eff} and ΔB_{FWHM} values. This is because three-dimensional magnetostatic interactions affect the effective field and also cause Gaussian line broadening due to the heterogeneity of local magnetic environments produced by interactions [*Kopp et al.*, 2006b]. Compared to SD grains with the same composition, SP grains with relaxation times smaller than the Larmor precession period have g_{eff} values close to their intrinsic value and A close to 1, which can be explained by thermally induced magnetization fluctuations averaging out the magnetic anisotropy field over a precession period [*Sharma and Baiker*, 1981]. The lack of anisotropy in SP grains also reduces ΔB_{FWHM}. The linewidth of SP materials broadens with decreasing temperature because of the diminishing influence of thermal fluctuations. MD grains tend to increase g_{eff}, A and ΔB_{FWHM} values due to absorption of microwave energy by domain walls at relatively low field strengths where domain walls still exist. Sample heterogeneity normally increases g_{eff} and ΔB_{FWHM}, but seems not to affect A [*Kopp et al.*, 2006a]. It should be noted that the effects of both three-dimensional magnetostatic interactions and domain structure on the FMR line shape are not well understood yet. More work is needed to better explain these effects.

[30] FMR spectra for greigite are broad with linewidths between ~180 and 240 mT at X-band at room temperature. Pure synthetic PSD/MD greigite samples have high g_{eff} values (2.9–3.1) and asymmetry ratio $A > 1$ (1.2–1.4). MD grains tend to decrease the effective absorption field (i.e., increase g_{eff}, see paragraph above). Sedimentary (diagenetic) greigite produces lower g_{eff} values (2.0–2.2), lower linewidths, and A values less than 1 (~0.7–0.9), which sometimes fall within the range of some parameters that have been used as indicators of the presence of magnetite magnetofossils ($A < 1$ and $g_{eff} < 2.12$). g_{eff} values are almost indistinguishable

for all of the measured greigite samples at Q-band (2.08–2.12). Compared to greigite, pyrrhotite has strong uniaxial anisotropy, which requires very high frequency (e.g., W-band) to acquire a full FMR absorption spectrum. This is consistent with the weak measured FMR signals at X- and Q-bands, which probably reflect effects of magnetic domain walls, defects, and impurities, rather than intrinsic properties of pyrrhotite. FMR fingerprints at X-band may be diagnostic of pyrrhotite and greigite.

[31] The TC tuff samples with non-interacting titanomagnetite grains give rise to multiple local absorption maxima and minima with lower g_{eff} (2.03–2.06), ΔB_{FWHM} (232–243 mT) and A values (0.66–0.78) than magnetically interacting samples. These FMR features can be predicted by modeling elongated TM10 grains. Measurements of synthetic magnetite chains do not give rise to FMR signatures that are characteristic of magnetosome chains although magnetite chains are present. Three-dimensional magnetostatic interactions among the magnetite chains can apparently mask the chain signal. Our FMR data demonstrate that g_{eff}, ΔB_{FWHM} and A decrease with decreasing magnetostatic interactions. The multiple absorption maxima in the FMR spectra with $A < 1$ and $g_{eff} < 2.12$ result from a combination of enhanced shape anisotropy effects and a lack of magnetic interactions. Our results demonstrate that samples with asymmetric FMR spectra with extended absorption at low fields need not necessarily contain magnetosome chains. Despite the large overlap in a range of FMR signatures between intact magnetite magnetosome chains and the samples analyzed here, magnetite magnetosome chains still have some distinct FMR characteristics (i.e., ΔB_{FWHM} and α values). Intact magnetosome chains therefore remain a rather unique FMR model system [*Weiss et al.*, 2004; *Kopp et al.*, 2006a, 2006b; *Charilaou et al.*, 2011]. Our results support previous studies that concluded that FMR analysis provides a powerful tool for identifying magnetite magnetosome chains within samples [e.g., *Weiss et al.*, 2004; *Kopp et al.*, 2006a, 2007, 2009; *Fischer et al.*, 2008; *Faivre et al.*, 2010; *Kind et al.*, 2011; *Roberts et al.*, 2011a; *Gehring et al.*, 2011a].

[32] While FMR analysis is useful for characterizing magnetic minerals in natural samples, care is needed when interpreting results because of the overlapping ranges of FMR parameters for different magnetic minerals with different properties. It is therefore not straightforward to interpret FMR signatures because of these overlapping effects. Ambiguity may also arise due to the complexity of natural magnetic samples. Nevertheless, the advantages of FMR analysis, such as its rapidity of measurement (it typically takes only several minutes to measure a sample) and inexpensiveness, make it possible to screen large numbers of samples to provide valuable magnetic information about samples.

Acknowledgments

[33] All FMR spectra were measured at the EPR National Service Centre at the University of Manchester, which is funded by the UK Engineering and Physical Sciences Research Council (EPSRC), and at the Research School of Earth Sciences, Australian National University. We thank Joanna Wolowska and Rainer Grün for help with measurements. We thank Mike Jackson at the Institute for Rock Magnetism for providing the TC Tuff samples. We are grateful to Bob Kopp, an anonymous reviewer and the Associate Editor for comments that significantly improved this paper. This work was partially funded through U.K. Natural Environment Research Council (NERC) grant NE/G003319/1 to APR.

References

Bazylinski, D. A., and R. B. Frankel (2004), Magnetosome formation in prokaryotes, *Nat. Rev. Microbiol.*, *2*, 217–230, doi:10.1038/nrmicro842.

Bazylinski, D. A., R. B. Frankel, B. R. Heywood, S. Mann, J. W. King, P. L. Donaghay, and A. K. Hanson (1995), Controlled biomineralization of magnetite (Fe_3O_4) and greigite (Fe_3S_4) in a magnetotactic bacterium, *Appl. Environ. Microbiol.*, *61*, 3232–3239.

Bickford, L. R., Jr. (1950), Ferromagnetic resonance absorption in magnetite single crystals, *Phys. Rev.*, *78*, 449–457, doi:10.1103/PhysRev.78.449.

Bin, M., and R. Pauthenet (1963), Magnetic anisotropy in pyrrhotite, *J. Appl. Phys.*, *34*, 1161–1162, doi:10.1063/1.1729413.

Carter-Stiglitz, B. S., P. A. Solheid, R. Egli, and A. P. Chen (2006), Tiva Canyon Tuff (II), *IRM Q.*, *16*, 1–10.

Chang, L., A. P. Roberts, A. R. Muxworthy, Y. Tang, Q. Chen, C. J. Rowan, Q. Liu, and P. Pruner (2007), Magnetic characteristics of synthetic pseudo-single-domain and multi-domain greigite (Fe_3S_4), *Geophys. Res. Lett.*, *34*, L24304, doi:10.1029/2007GL032114.

Chang, L., A. P. Roberts, Y. Tang, B. D. Rainford, A. R. Muxworthy, and Q. Chen (2008), Fundamental magnetic parameters from pure synthetic greigite (Fe_3S_4), *J. Geophys. Res.*, *113*, B06104, doi:10.1029/2007JB005502.

Chang, L., B. D. Rainford, J. R. Stewart, C. Ritter, A. P. Roberts, Y. Tang, and Q. Chen (2009a), Magnetic structure of greigite (Fe_3S_4) probed by neutron powder diffraction and polarized neutron diffraction, *J. Geophys. Res.*, *114*, B07101, doi:10.1029/2008JB006260.

Chang, L., A. P. Roberts, C. J. Rowan, Y. Tang, P. Pruner, Q. Chen, and C. S. Horng (2009b), Low-temperature magnetic properties of greigite (Fe_3S_4), *Geochem. Geophys. Geosyst.*, *10*, Q01Y04, doi:10.1029/2008GC002276.

Charilaou, M., M. Winklhofer, and A. U. Gehring (2011), Simulation of ferromagnetic resonance spectra of linear chains of magnetite nano-crystals, *J. Appl. Phys.*, *109*, 093903, doi:10.1063/1.3581103.

Crook, N. P., S. R. Hoon, K. G. Taylor, and C. T. Perry (2002), Electron spin resonance as a high sensitivity technique for environmental magnetism: Determination of contamination in carbonate sediments, *Geophys. J. Int.*, *149*, 328–337, doi:10.1046/j.1365-246X.2002.01647.x.

Dekkers, M. J. (1988), Magnetic properties of natural pyrrhotite part I: Behaviour of initial susceptibility and saturation-magnetization-related rock-magnetic parameters in a grain-size dependent framework, *Phys. Earth Planet. Inter.*, *52*, 376–393, doi:10.1016/0031-9201(88)90129-X.

Dekkers, M. J., and M. A. A. Schoonen (1996), Magnetic properties of hydrothermally synthesised greigite (Fe_3S_4)—I. Rock magnetic parameters at room temperature, *Geophys. J. Int.*, *126*, 360–368, doi:10.1111/j.1365-246X.1996.tb05296.x.

Faivre, D., A. Fischer, I. Garcia-Rubio, G. Mastrogiacomo, and A. U. Gehring (2010), Development of cellular magnetic dipoles in magnetotactic bacteria, *Biophys. J.*, *99*, 1268–1273, doi:10.1016/j.bpj.2010.05.034.

Fischer, H., J. Luster, and A. U. Gehring (2007), EPR evidence for maghemitization of magnetite in a tropical soil, *Geophys. J. Int.*, *169*, 909–916, doi:10.1111/j.1365-246X.2007.03311.x.

Fischer, H., G. Mastrogiacomo, J. F. Löffler, R. J. Warthmann, P. G. Weidler, and A. U. Gehring (2008), Ferromagnetic resonance and magnetic characteristics of intact magnetosome chains in *Magnetospirillum gryphiswaldense*, *Earth Planet. Sci. Lett.*, *270*, 200–208, doi:10.1016/j.epsl.2008.03.022.

Fujimura, T., and Y. Torizuka (1956), Ferromagnetic resonance absorption in a pyrrhotite single crystal, *J. Phys. Soc. Jpn.*, *11*, 327, doi:10.1143/JPSJ.11.327.

Gehring, A. U., J. Kind, M. Charilaou, and I. García-Rubio (2011a), The detection of magnetotactic bacteria and magnetofossils by means of magnetic anisotropy, *Earth Planet. Sci. Lett.*, *309*, 113–117, doi:10.1016/j.epsl.2011.06.024.

Gehring, A. U., H. Fischer, M. Charilaou, and I. García-Rubio (2011b), Magnetic anisotropy and Verwey transition of magnetosome chains in *Magnetospirillum gryphiswaldense*, *Geophys. J. Int.*, *187*, 1215–1221, doi:10.1111/j.1365-246X.2011.05175.x.

Griscom, D. L. (1974), Ferromagnetic resonance spectra of lunar fines: Some implications of line shape analysis, *Geochim. Cosmochim. Acta*, *38*, 1509–1519, doi:10.1016/0016-7037(74)90171-9.

Griscom, D. L. (1980), Ferromagnetic resonance of fine grained precipitates in glass: A thumbnail review, *J. Non Cryst. Solids*, *42*, 287–296, doi:10.1016/0022-3093(80)90030-7.

Hofmeister, A. M., and G. R. Rossman (1984), Determination of Fe^{3+} and Fe^{2+} concentrations in feldspar by optical absorption and EPR spectroscopy, *Phys. Chem. Miner.*, *11*, 213–224, doi:10.1007/BF00308136.

Horng, C. S., and C. A. Huh (2011), Magnetic properties as tracers for source-to-sink dispersal of sediments: A case study in the Taiwan Strait, *Earth Planet. Sci. Lett.*, *309*, 141–152.

Horng, C. S., and A. P. Roberts (2006), Authigenic or detrital origin of pyrrhotite in sediments? Resolving a paleomagnetic conundrum, *Earth Planet. Sci. Lett.*, *241*, 750–762, doi:10.1016/j.epsl.2005.11.008.

Hüsing, S. K., M. J. Dekkers, C. Franke, and W. Krijgsman (2009), The Tortonian reference section at Monte dei Corvi (Italy): Evidence for early remanence acquisition in greigite-bearing sediments, *Geophys. J. Int.*, *179*, 125–143, doi:10.1111/j.1365-246X.2009.04301.x.

Jackson, M., B. Carter-Stiglitz, R. Egli, and P. Solheid (2006), Characterizing the superparamagnetic grain distribution f(V, H_k) by thermal fluctuation tomography, *J. Geophys. Res.*, *111*, B12S07, doi:10.1029/2006JB004514.

Jiang, W. T., C. S. Horng, A. P. Roberts, and D. R. Peacor (2001), Contradictory magnetic polarities in sediments and variable timing of neoformation of authigenic greigite, *Earth Planet. Sci. Lett.*, *193*, 1–12, doi:10.1016/S0012-821X(01)00497-6.

Kakol, Z., and J. M. Honig (1989), Influence of deviations from ideal stoichiometry on the anisotropy parameters of magnetite $Fe_{3(1-\delta)}O_4$, *Phys. Rev. B*, *40*, 9090–9097, doi:10.1103/PhysRevB.40.9090.

Kakol, Z., J. Sabol, and J. M. Honig (1991), Magnetic anisotropy of titanomagnetites $Fe_{3-x}Ti_xO_4$, $0 \le x \le 0.55$, *Phys. Rev. B*, *44*, 2198–2204.

Kind, J., A. U. Gehring, M. Winklhofer, and A. M. Hirt (2011), Combined use of magnetometry and spectroscopy for identifying magnetofossils in sediments, *Geochem. Geophys. Geosyst.*, *12*, Q08008, doi:10.1029/2011GC003633.

Kittel, C. (1996), *Introduction to Solid State Physics*, 7th ed., John Wiley, New York.

Konhauser, K. O. (1998), Diversity of bacterial iron mineralization, *Earth Sci. Rev.*, *43*, 91–121, doi:10.1016/S0012-8252(97)00036-6.

Koonce, C. S., B. W. Mangum, and D. D. Thornton (1971), Magnetic properties of the antiferromagnet $DyPO_4$ in applied fields, *Phys. Rev. B*, *4*, 4054–4069, doi:10.1103/PhysRevB.4.4054.

Kopp, R. E., and J. L. Kirschvink (2008), The identification and biogeochemical interpretation of fossil magnetotactic bacteria, *Earth Sci. Rev.*, *86*, 42–61.

Kopp, R. E., B. P. Weiss, A. C. Maloof, H. Vali, C. Z. Nash, and J. L. Kirschvink (2006a), Chains, clumps, and strings: Magnetofossil taphonomy with ferromagnetic resonance spectroscopy, *Earth Planet. Sci. Lett.*, *247*, 10–25, doi:10.1016/j.epsl.2006.05.001.

Kopp, R. E., C. Z. Nash, A. Kobayashi, B. P. Weiss, D. A. Bazylinski, and J. L. Kirschvink (2006b), Ferromagnetic resonance spectroscopy for assessment of magnetic anisotropy and magnetostatic interactions: A case study of mutant magnetotactic bacteria, *J. Geophys. Res.*, *111*, B12S25, doi:10.1029/2006JB004529.

Kopp, R. E., T. D. Raub, D. Schumann, H. Vali, A. V. Smirnov, and J. L. Kirschvink (2007), Magnetofossil spike during the Paleocene-Eocene thermal maximum: Ferromagnetic resonance, rock magnetic, and electron microscopy evidence from Ancora, New Jersey, United States, *Paleoceanography*, *22*, PA4103, doi:10.1029/2007PA001473.

Kopp, R. E., D. Schumann, T. D. Raub, D. S. Powars, L. V. Godfrey, N. L. Swanson-Hysell, A. C. Maloof, and H. Vali (2009), An Appalachian Amazon? Magnetofossil evidence for the development of a tropical river-like system in the mid-Atlantic United States during the Paleocene-Eocene Thermal Maximum, *Paleoceanography*, *24*, PA4211, doi:10.1029/2009PA001783.

Liu, Y., and Q. Chen (2008), Synthesis of magnetosome chain-like structures, *Nanotechnology*, *19*, 475603, doi:10.1088/0957-4484/19/47/475603.

Maloof, A. C., R. E. Kopp, J. P. Grotzinger, D. A. Fike, T. Bosak, H. Vali, P. M. Poussart, B. P. Weiss, and J. L. Kirschvink (2007), Sedimentary iron cycling and the origin and preservation of magnetization in platform carbonate muds, Andros Island, Bahamas, *Earth Planet. Sci. Lett.*, *259*, 581–598, doi:10.1016/j.epsl.2007.05.021.

Martín-Hernández, F., M. J. Dekkers, I. M. A. Bominaar-Silkens, and J. C. Maan (2008), Magnetic anisotropy behaviour of pyrrhotite as determined by low- and high-field experiments, *Geophys. J. Int.*, *174*, 42–54, doi:10.1111/j.1365-246X.2008.03793.x.

Mastrogiacomo, G., H. Fischer, I. García-Rubio, and A. U. Gehring (2010), Ferromagnetic resonance spectroscopic response of magnetite chains in a biological matrix, *J. Magn. Magn. Mater.*, *322*, 661–663, doi:10.1016/j.jmmm.2009.10.035.

Mikhlin, Y. L., A. V. Kuklinskiy, N. I. Pavlenko, V. A. Varnek, I. P. Asanov, A. V. Okotrub, G. E. Selyutin, and L. A. Solovyev (2002), Spectroscopic and XRD studies of the air degradation of acid-reacted pyrrhotites, *Geochim. Cosmochim. Acta*, *66*, 4057–4067, doi:10.1016/S0016-7037(02)00989-4.

Pawse, A., S. Beske-Diehl, and S. A. Marshall (1998), Use of magnetic hysteresis properties and electron spin resonance spectroscopy for the identification of volcanic ash: A preliminary study, *Geophys. J. Int.*, *132*, 712–720, doi:10.1046/j.1365-246X.1998.00487.x.

Pearce, C. I., R. A. D. Pattrick, and D. J. Vaughan (2006), Electrical and magnetic properties of sulfides, *Rev. Mineral. Geochem.*, *61*, 127–180, doi:10.2138/rmg.2006.61.3.

Roberts, A. P. (1995), Magnetic characteristics of sedimentary greigite (Fe_3S_4), *Earth Planet. Sci. Lett.*, *134*, 227–236, doi:10.1016/0012-821X(95)00131-U.

Roberts, A. P., and R. Weaver (2005), Multiple mechanisms of remagnetization involving sedimentary greigite (Fe_3S_4), *Earth Planet. Sci. Lett.*, *231*, 263–277, doi:10.1016/j.epsl.2004.11.024.

Roberts, A. P., C. R. Pike, and K. L. Verosub (2000), First-order reversal curve diagrams: A new tool for characterizing the magnetic properties of natural samples, *J. Geophys. Res.*, *105*, 28,461–28,475, doi:10.1029/2000JB900326.

Roberts, A. P., Q. Liu, C. J. Rowan, L. Chang, C. Carvallo, J. Torrent, and C. S. Horng (2006), Characterization of hematite (α-Fe_2O_3), goethite (α-FeOOH), greigite (Fe_3S_4), and pyrrhotite (Fe_7S_8) using first-order reversal curve diagrams, *J. Geophys. Res.*, *111*, B12S35, doi:10.1029/2006JB004715.

Roberts, A. P., F. Florindo, G. Villa, L. Chang, L. Jovane, S. M. Bohaty, J. C. Larrasoaña, D. Heslop, and J. D. Fitz Gerald (2011a), Magnetotactic bacterial abundance in pelagic marine environments is limited by organic carbon flux and availability of dissolved iron, *Earth Planet. Sci. Lett.*, *310*, 441–452, doi:10.1016/j.epsl.2011.08.011.

Roberts, A. P., L. Chang, C. J. Rowan, C.-S. Horng, and F. Florindo (2011b), Magnetic properties of sedimentary greigite (Fe_3S_4): An update, *Rev. Geophys.*, *49*, RG1002, doi:10.1029/2010RG000336.

Rochette, P. (1987), Metamorphic control of the magnetic mineralogy of black shales in the Swiss Alps: Toward the use of "magnetic isograds," *Earth Planet. Sci. Lett.*, *84*, 446–456, doi:10.1016/0012-821X(87)90009-4.

Rochette, P., J.-P. Lorand, G. Fillion, and V. Sautter (2001), Pyrrhotite and the remanent magnetization of SNC meteorites: A changing perspective on Martian magnetism, *Earth Planet. Sci. Lett.*, *190*, 1–12, doi:10.1016/S0012-821X(01)00373-9.

Rosenbaum, J. G. (1993), Magnetic grain-size variations through an ash flow sheet: Influence on magnetic properties and implications for cooling history, *J. Geophys. Res.*, *98*, 11,715–11,727, doi:10.1029/93JB00355.

Sagnotti, L., and A. Winkler (1999), Rock magnetism and palaeomagnetism of greigite-bearing mudstones in the Italian peninsula, *Earth Planet. Sci. Lett.*, *165*, 67–80, doi:10.1016/S0012-821X(98)00248-9.

Sagnotti, L., A. Cascella, N. Ciaranfi, P. Macrì, P. Maiorano, M. Marino, and J. Taddeucci (2010), Rock magnetism and palaeomagnetism of the Montalbano Jonico section (Italy): Evidence for late diagenetic growth of greigite and implications for magnetostratigraphy, *Geophys. J. Int.*, *180*, 1049–1066, doi:10.1111/j.1365-246X.2009.04480.x.

Schlinger, C. M., D. R. Veblen, and J. G. Rosenbaum (1991), Magnetism and magnetic mineralogy of ash flow tuffs from Yucca Mountain, Nevada, *J. Geophys. Res.*, *96*, 6035–6052, doi:10.1029/90JB02653.

Sharma, V. K., and A. Baiker (1981), Superparamagnetic effects in the ferromagnetic resonance of silica supported nickel particles, *J. Chem. Phys.*, *75*, 5596–5601, doi:10.1063/1.441997.

Suzuki, Y., et al. (2006), Sclerite formation in the hydrothermal vent "scaly-foot" gastropod—Possible control of iron sulfide biomineralization by the animal, *Earth Planet. Sci. Lett.*, *242*, 39–50, doi:10.1016/j.epsl.2005.11.029.

Syono, Y., and Y. Ishikawa (1963), Magnetocrystalline anisotropy of $x$$Fe_2TiO_4$ (1–x) Fe_3O_4, *J. Phys. Soc. Jpn.*, *18*, 1230–1231, doi:10.1143/JPSJ.18.1230.

Tang, Y., Q. W. Chen, Y. Xiong, and Y. Li (2007), Magnetic field-induced increase in conversion rate of Fe_3S_4 to FeS_2, *Chin. J. Inorg. Chem.*, *23*, 941–947.

Till, J. L., M. J. Jackson, J. G. Rosenbaum, and P. Solheid (2011), Magnetic properties in an ash flow tuff with continuous grain size variation: A natural reference for magnetic particle granulometry, *Geochem. Geophys. Geosyst.*, *12*, Q07Z26, doi:10.1029/2011GC003648.

Valstyn, E. P., J. P. Hanton, and A. H. Morrish (1962), Ferromagnetic resonance of single-domain particles, *Phys. Rev.*, *128*, 2078–2087, doi:10.1103/PhysRev.128.2078.

van Dongen, B. E., A. P. Roberts, S. Schouten, W. T. Jiang, F. Florindo, and R. D. Pancost (2007), Formation of iron sulfide nodules during anaerobic oxidation of methane, *Geochim. Cosmochim. Acta*, *71*, 5155–5167, doi:10.1016/j.gca.2007.08.019.

Vasiliev, I., M. J. Dekkers, W. Krijgsman, C. Franke, C. G. Langereis, and T. A. T. Mullender (2007), Early diagenetic greigite as a recorder of the palaeomagnetic signal in Miocene-Pliocene sedimentary rocks of the Carpathian foredeep (Romania), *Geophys. J. Int.*, *171*, 613–629, doi:10.1111/j.1365-246X.2007.03560.x.

Vasiliev, I., C. Franke, J. D. Meeldijk, M. J. Dekkers, C. G. Langereis, and W. Krijgsman (2008), Putative greigite magnetofossils from the Pliocene Epoch, *Nat. Geosci.*, *1*, 782–786, doi:10.1038/ngeo335.

Weaver, R., A. P. Roberts, and A. J. Barker (2002), A late diagenetic (syn-folding) magnetization carried by pyrrhotite: Implications for paleomagnetic studies from magnetic iron sulphide-bearing sediments, *Earth Planet. Sci. Lett.*, *200*, 371–386, doi:10.1016/S0012-821X(02)00652-0.

Wehland, F., A. Stancu, P. Rochette, M. J. Dekkers, and E. Appel (2005), Experimental evaluation of magnetic interaction in pyrrhotite bearing samples, *Phys. Earth Planet. Inter.*, *153*, 181–190, doi:10.1016/j.pepi.2005.05.006.

Weiss, B. P., S. S. Kim, J. L. Kirschvink, R. E. Kopp, M. Sankaran, A. Kobayashi, and A. Komeili (2004), Ferromagnetic resonance and low temperature magnetic tests for biogenic magnetite, *Earth Planet. Sci. Lett.*, *224*, 73–89, doi:10.1016/j.epsl.2004.04.024.

Worm, H.-U., and M. Jackson (1999), The superparamagnetism of Yucca Mountain Tuff, *J. Geophys. Res.*, *104*, 25,415–25,425, doi:10.1029/1999JB900285.

Yamaguchi, S., and H. Wada (1970), Magnetic anisotropy of Fe_3S_4 as revealed by electron diffraction, *J. Appl. Phys.*, *41*, 1873–1874, doi:10.1063/1.1659128.

Ye, J., A. J. Newell, and R. T. Merrill (1994), A re-evaluation of magnetocrystalline anisotropy and magnetostriction constants, *Geophys. Res. Lett.*, *21*, 25–28, doi:10.1029/93GL03263.